Effects of Mg and Sb Substitution on the Magnetic Properties of Magnetic Field Annealed MnBi Alloys

Hui-Dong Qian [1,2], **Yang Yang** [1,2], **Jung Tae Lim** [1], **Jong-Woo Kim** [1], **Chul-Jin Choi** [1,*] **and Jihoon Park** [1,*]

[1] Powder & Ceramics Division, Korea Institute of Materials Science, Changwon 51508, Korea; qianhuidong@kims.re.kr (H.-D.Q.); yangyang@kims.re.kr (Y.Y.); jungtae0401@kims.re.kr (J.T.L.); jwk@kims.re.kr (J.-W.K.)

[2] School of Materials Science and Engineering, Pusan National University, Busan 46241, Korea

[*] Correspondence: cjchoi@kims.re.kr (C.-J.C.); jpark@kims.re.kr (J.P.)

check for updates

Abstract: Rare-earth-free permanent magnets have attracted considerable attention due to their favorable properties and applicability for cost-effective, high-efficiency, and sustainable energy devices. However, the magnetic field annealing process, which enhances the performance of permanent magnets, needs to be optimized for different magnetic fields and phases. Therefore, we investigated the effect of composition on the crystallization of amorphous MnBi to the ferromagnetic low-temperature phase(LTP). The optimal compositions and conditions were applied to magnetic field annealing under 2.5 T for elemental Mg- and Sb/Mg pair-substituted MnBi. The optimum MnBi composition for the highest purity LTP was determined to be $Mn_{56}Bi_{44}$, and its maximum energy product, $(BH)_{max}$, was 5.62 MGOe. The Mg-substituted MnBi exhibited enhanced squareness (M_r/M_s), coercivity (H_c), and $(BH)_{max}$ values up to 0.8, 9659 Oe, and 5.64 MGOe, respectively, whereas the same values for the Sb/Mg pair-substituted MnBi were 0.76, 7038 Oe, and 5.60 MGOe, respectively. The substitution effects were also investigated using first-principles calculations. The density of states and total magnetic moments of $Mn_{16}Bi_{15}Mg$ and $Mn_{16}Bi_{15}Sb$ were similar to those of pure $Mn_{16}Bi_{16}$. Conversely, the Sb-substituted MnBi resulted in a dramatic enhancement in the anisotropy constant (K) from a small negative value (-0.85 MJ/m^3) to a large positive value (6.042 MJ/m^3).

Keywords: MnBi; Mg substitution; Sb substitution; magnetic properties; magnetic field annealing

1. Introduction

Rare-earth-free permanent magnets featuring high maximum energy products ($(BH)_{max}$) between those of rare-earth and traditional rare-earth-free permanent magnets are in high demand for cost-effective, high-efficiency, and sustainable energy devices [1,2]. Among rare-earth-free permanent magnetic materials, MnBi exhibits the most promising magnetic properties, featuring high $(BH)_{max}$ values that exceed 9 MGOe for powder [3–7] and 7 MGOe for bulk [7–10]. Notably, the theoretical $(BH)_{max}$ of MnBi is 17.7 MGOe at 300 K [11]. During compaction of the powder samples, the reduced coercivity (H_c) degrades the $(BH)_{max}$ for bulk MnBi. Consequently, the addition of secondary elements or materials, such as Ga (e.g., $Mn_{55}Bi_{44}Ga$) [12], Sn (e.g., $MnBi_{1-x}Sn_x$) [13], NaCl or C [14], and nanoparticles [15], to MnBi has been investigated in efforts to increase the H_c. Furthermore, magnetic field annealing has been used to enhance the magnetic properties for permanent magnet applications [16–21].

Magnetic field annealing, a process widely used to fabricate Alnico magnets [22], induces aligned texturing in the microstructure. However, the process is not efficient for all permanent magnets owing to variations in the field dependence of the magnetic phase crystallization. Secondary elements such as Sn, Sb, Mg, and In have been substituted/doped to enhance the effectiveness of field

annealing for MnBi permanent magnetic materials [23–27]. The magnetic properties of the secondary element-doped/substituted MnBi are superior to those of MnBi fabricated using a field annealing process, revealing higher magnetization, H_c, and squareness (M_r/M_s) than those of binary MnBi [23–27]. Therefore, the highest $(BH)_{max}$ (12 MGOe) was achieved for $Mn_{50}Bi_{46}Mg_3In_{0.5}Sb_{0.5}$ bulk magnetic material [27].

In this study, we systematically investigated the composition ($Mn_{52+x}Bi_{48-x}$, $0 \leq x \leq 8$) and annealing condition dependencies of the purity of the low-temperature phase (LTP). The optimized composition was used in magnetic field annealing experiments under the optimized annealing conditions with an applied field of 2.5 T. The dependence of the magnetic properties on the substitution of Mg and Sb/Mg pairs over large composition ranges, i.e., $Mn_{56}Bi_{44-x}Mg_x$ ($0 \leq x \leq 5$) and $Mn_{56}Bi_{43.5-x}Sb_{0.5}Mg_x$ ($0 \leq x \leq 5$), were also systematically investigated. To better comprehend the experimental data, the substitution effects were analyzed using total energies based on different spin configurations, densities of states (DOSs), and magnetic moments.

2. Experimental and Calculations

MnBi, Mn-Bi-Mg, and Mn-Bi-Sb-Mg bulks were prepared using the following procedure: melt spinning, cold pressing, and magnetic annealing. The commercial raw materials of Mn (99.95%), Bi (99.999%), Mg (99.98%), and Sb (99.999%) were mixed in the desired atomic ratios of $Mn_{52+x}Bi_{48-x}$ ($0 \leq x \leq 8$), $Mn_{56}Bi_{44-x}Mg_x$ ($0 \leq x \leq 5$), and $Mn_{56}Bi_{43.5-x}Sb_{0.5}Mgx$ ($0 \leq x \leq 5$). The mixtures were melted in an Ar environment in quartz nozzles and ejected through a 0.4 mm orifice using pressurized Ar gas onto a copper wheel rotating at a velocity of 40 m/s. The melt-spun ribbons were manually ground (5 min) in ethyl alcohol and then pressed into pellets in tungsten carbide molds (500 MPa). The produced pellets were cut into small pieces (1.5 mm × 1.0 mm × 3 mm) and subjected to magnetic annealing under a magnetic field of 2.5 T. The annealing temperature was optimized by measuring the temperature dependence of the magnetic moment of an amorphous bulk, where the ramping rate was maintained at 16 °C/min. Once the temperature reached the target temperature, the heating element was immediately removed to rapidly cool the samples.

The crystalline structures and phase purities of the products were characterized using X-ray diffraction (XRD) with Cu Kα (λ = 1.5406 Å) radiation (Rigaku Inc., D/Max-2500VL/PC, Tokyo, Japan). Further, the measured XRD patterns were analyzed using the Rietveld refinement method with the program FullProf. Magnetic annealing and magnetic property measurements were performed using a vibrating sample magnetometer (VSM) (Microsense, EZ9, Lowell, MA, USA). The magnetic properties of the bulk samples were corrected according to their shape with a demagnetization factor of 0.1655.

The WIEN2k package [28] was used to perform first-principles calculations. The package is based on density functional theory (DFT) and uses the full-potential linearized augmented plane wave method. The 3p, 3d, and 4s states of Mn; 4d, 4f, 5p, 5d, 6s, and 6p states of Bi; 3s state of Mg; and 4p, 4d, 5s, and 5p states of Sb were treated as valence states in the calculations. Unit cell and supercell calculations used 28 × 28 × 24 and 25 × 25 × 15 reciprocal space meshes, which generate 18,816 and 9375 k-points in the irreducible part of the Brillouin zone, respectively. The total energies were calculated within an accuracy of 0.0013 eV. The experimental lattice constants (a = 4.256 Å and c = 6.042 Å at 4.2 K) [29] in Figure 1 were used, and the muffin-tin radii (RMT) for Mn, Bi, Mg, and Sb were set as 2.5 a.u. The cutoff parameter of PMT × K_{max} = 7.0 with l_{max} = 10 inside the muffin-tin spheres was used to expand the wavefunctions in terms of the lattice harmonics. All spin-polarized and spin-orbit coupling calculations were based on DFT within the local-spin-density approximation (LSDA).
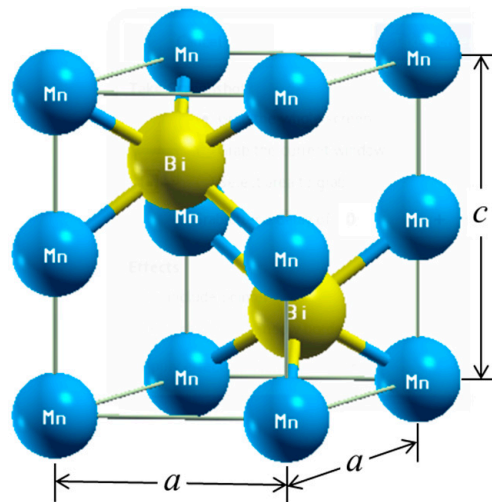
Figure 1. Hexagonal low-temperature phase (LTP) MnBi. The Mn and Bi atoms are blue and yellow, respectively.

3. Results and Discussion

The degree of amorphization plays an important role in crystallizing LTP $Mn_{50}Bi_{50}$ in the direction of the magnetic field. Therefore, we prepared $Mn_{52+x}Bi_{48-x}$ ($0 \leq x \leq 8$) samples to investigate the composition dependence of the degree of amorphization and their crystallization to LTP $Mn_{50}Bi_{50}$ after annealing at 300 °C for 24 h. Melt-spun $Mn_{52+x}Bi_{48-x}$ ($0 \leq x \leq 8$) products contain small amounts of droplet-shaped particles and ribbons. These particles were removed, and only the ribbons were collected to fabricate bulk samples. It is noted that Mn and Bi were partially reacted with quartz nozzle during the melt-spinning process; therefore, the final compositions converge into $Mn_{50}Bi_{50}$ regardless of the initial compositions. The bulks were loaded into a vacuum tube furnace and annealed. Figure 2a shows the XRD patterns of the $Mn_{52+x}Bi_{48-x}$ ($0 \leq x \leq 8$) melt-spun ribbons. All the samples exhibited minor peaks of Bi, whereas LTP $Mn_{50}Bi_{50}$ was not detected. Therefore, the melt-spun ribbons mostly comprised an amorphous phase with a small quantity of Bi crystallites. The differences in the peak intensities of Bi for the five samples were indistinguishable, except for $Mn_{54}Bi_{46}$. Figure 2b shows the XRD patterns of the annealed $Mn_{52+x}Bi_{48-x}$ ($0 \leq x \leq 8$) bulk samples. The purities of the samples were initially enhanced with increasing x, but they were not enhanced significantly when $x \geq 4$; the calculated purities were 84%, 93%, 96%, 96%, and 97% for $x = 0$, 2, 4, 6, and 8, respectively. Therefore, we used the composition $x = 4$, i.e., $Mn_{56}Bi_{44}$, for the following experiment.

The annealing temperature of amorphous $Mn_{56}Bi_{44}$ was optimized using VSM. Figure 3 depicts the temperature dependence of the magnetic moment per Mn atom of an amorphous $Mn_{56}Bi_{44}$ bulk sample under an applied magnetic field of 2.5 T. The amorphous $Mn_{56}Bi_{44}$ bulk sample was heated from 130 to 550 °C while its magnetic moment was measured using VSM. The measured magnetic moment of the paramagnetic amorphous bulk sample initially decreased with increasing temperature but began increasing at 220 °C due to crystallization of the amorphous phase. The highest magnetic moment was measured at temperatures ranging from 310 to 340 °C. It is noted that further heating of the sample above 355 °C results in irreversible decomposition of LTP $Mn_{50}Bi_{50}$ into $Mn_{52}Bi_{48}$ + Bi [30]. Therefore, we selected an annealing temperature of 320 °C for the annealing process. Notably, the magnetic moment declined at temperatures between 430 and 460 °C, with a sharp decrease at 450 °C. This temperature is considerably higher than the phase transformation temperature (340–360 °C) of MnBi from LTP to the high-temperature phase (HTP) [29]. This temperature disagreement at high temperatures may be attributed to heat loss in the open heating circuit of the VSM system.
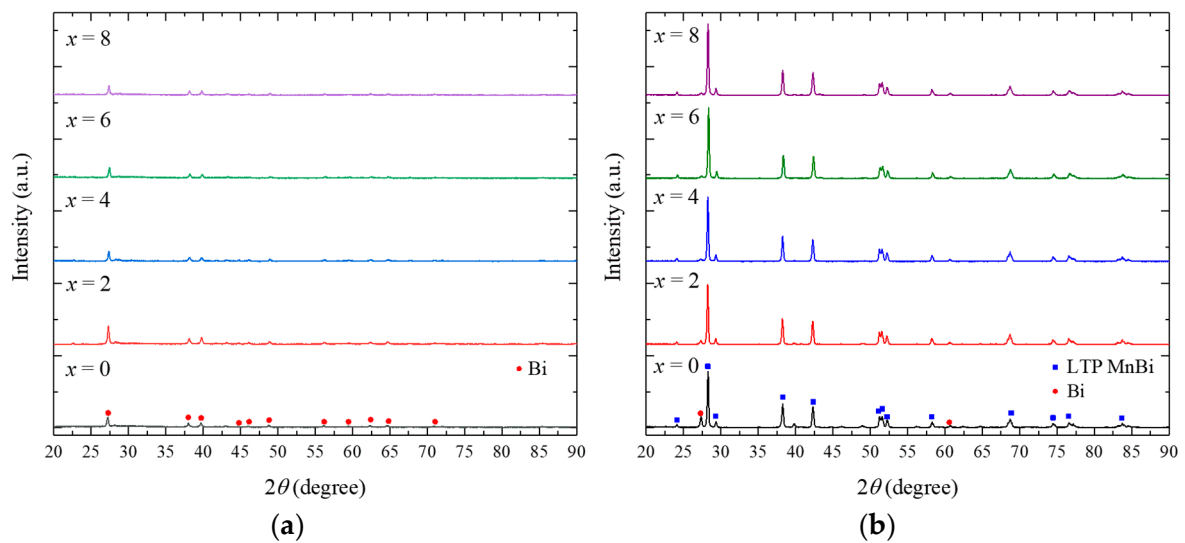
Figure 2. XRD patterns of the (**a**) ground $Mn_{52+x}Bi_{48-x}$ melt-spun ribbons and (**b**) annealed bulk samples (300 °C for 24 h).
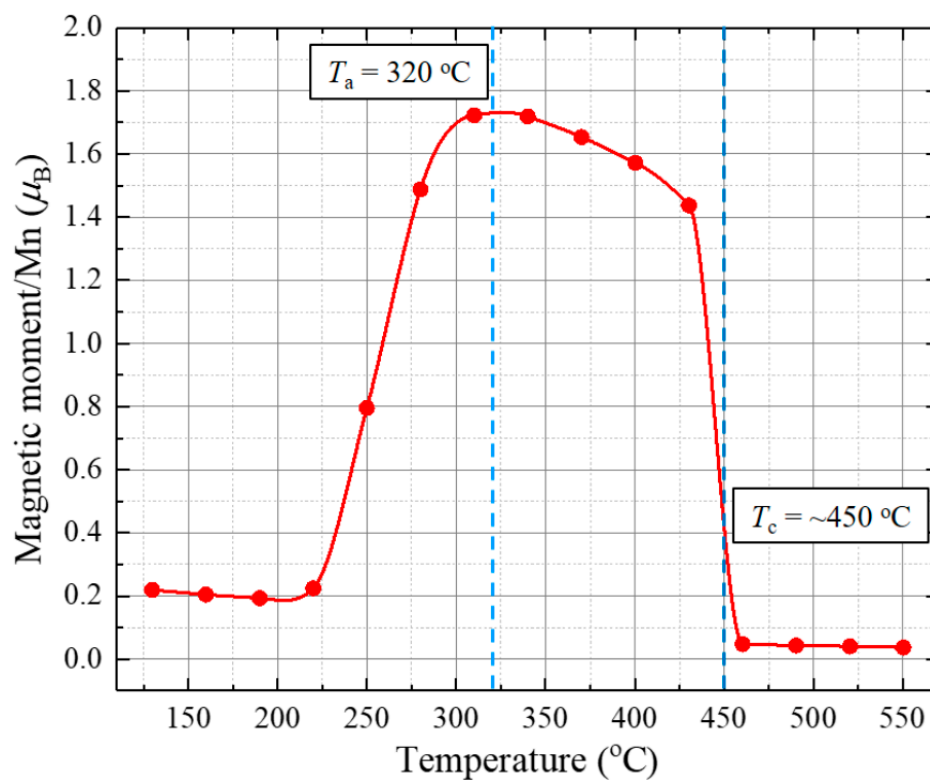

Figure 3. Temperature dependence of the magnetic moment per Mn atom of an amorphous $Mn_{56}Bi_{44}$ bulk sample under an applied magnetic field of 2.5 T.

Figure 4 depicts the refined XRD pattern of the $Mn_{56}Bi_{44}$ bulk sample annealed at 320 °C for 5 min. The phase identity and weight fraction were analyzed using the Rietveld refinement method with the program FullProf. The refined XRD pattern confirmed that the annealed $Mn_{56}Bi_{44}$ bulk had a hexagonal structure with a space group of $P6_3/mmc$, and the lattice constants a_0 and c_0 were 4.285 ± 0.001 and 6.113 ± 0.001 Å, respectively. The annealed $Mn_{56}Bi_{44}$ bulk mainly comprised the LTP, and the peak at approximately 27.24° corresponds to an impure Bi phase. After heat treatment at 320 °C

for 5 min, the purity of the LTP $Mn_{50}Bi_{50}$ increased to 98.15 wt.%. The Mn and Bi atoms occupied the 2a site (0, 0, 0) and the 2c site (1/3, 2/3, 1/4), respectively [31].
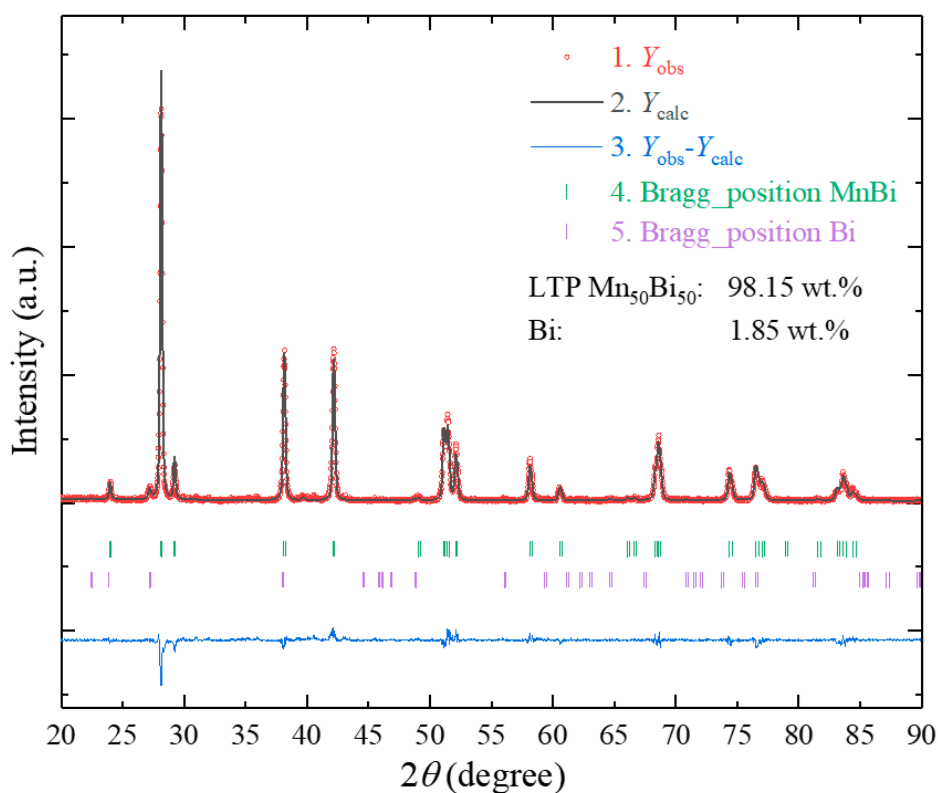

Figure 4. Refined XRD pattern of the annealed $Mn_{56}Bi_{44}$ bulk samples (320 °C for 5 min).

The magnetic hysteresis loops of the $Mn_{56}Bi_{44-x}Mg_x$ ($0 \leq x \leq 5$) bulk samples obtained after magnetic annealing under 2.5 T are shown in Figure 5. The hysteresis loops were smooth and did not contain any kinks until $x = 3$; however, a kink appeared at $x = 4$. As the Mg content increased, the magnetization at the maximum magnetic field and remanent magnetization decreased, whereas H_c increased to 9659 Oe for $x = 4$ and then decreased at higher values of x. The magnetization, squareness, H_c, and $(BH)_{max}$ of the $Mn_{56}Bi_{44-x}Mg_x$ ($0 \leq x \leq 5$) bulk samples are plotted in Figure 6. Although the magnetization at the maximum field and remanent magnetization decreased as x increased, $(BH)_{max}$ increased slightly from 5.62 MGOe (for $Mn_{56}Bi_{44}$) to 5.64 MGOe (for $Mn_{56}Bi_{43}Mg_1$ and $Mn_{56}Bi_{42}Mg_2$) because of the increased squareness ($M_r/M_s \approx 0.8$). At x values exceeding 2, $(BH)_{max}$ decreased linearly. The decreasing magnetization and increasing H_c for $x \geq 2$ originate from phase decomposition into nonmagnetic phases. The XRD patterns for the field-annealed samples will be published elsewhere. These impurities act as pinning centers for domain walls by strongly inhibiting their motion, thus reducing the efficiency of this reversal mechanism.
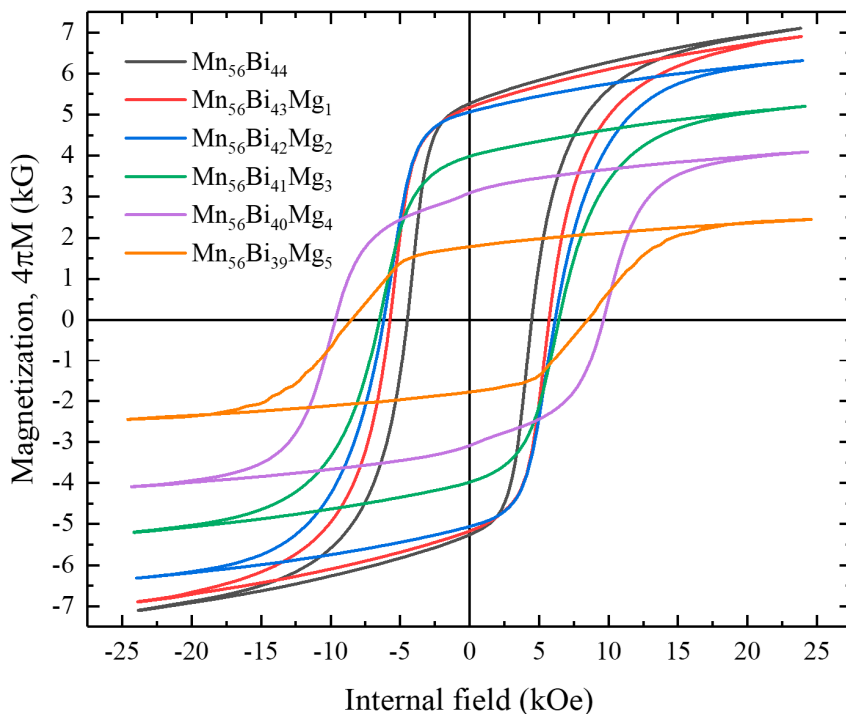
Figure 5. Magnetic hysteresis loops of $Mn_{56}Bi_{44-x}Mg_x$ ($0 \le x \le 5$) bulk samples.
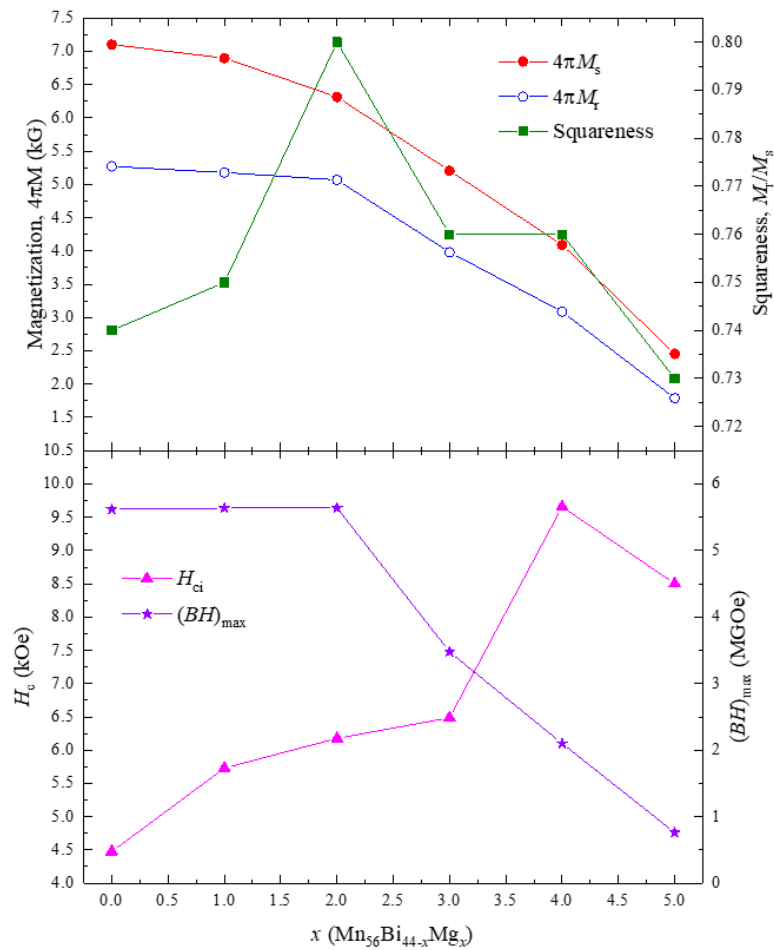

Figure 6. Composition dependence of magnetization, squareness, H_c, and $(BH)_{max}$ for the $Mn_{56}Bi_{44-x}Mg_x$ ($0 \le x \le 5$) bulk samples.

Sb-substituted Mn-Bi-Mg, i.e., $Mn_{56}Bi_{43.5-x}Sb_{0.5}Mg_x$ ($0 \leq x \leq 5$) bulk, was also fabricated to investigate the effect of Sb/Mg pair substitution on the magnetic properties. The magnetic hysteresis loops of the $Mn_{56}Bi_{43.5-x}Sb_{0.5}Mg_x$ ($0 \leq x \leq 5$) bulk samples are shown in Figure 7. The magnetic annealing process and conditions were the same as those for $Mn_{56}Bi_{44-x}Mg_x$ ($0 \leq x \leq 5$). The magnetization at maximum field and remanent magnetization decreased with increasing Mg content, while H_c linearly increased until $x = 4$, reaching 7038 Oe, as shown in Figure 8. The hysteresis loops were smooth, containing no kinks until $x = 3$, but a kink appeared at $x = 4$. Substitution of a small amount of Sb into Mn-Bi-Mg increased H_c until $x = 3$ but caused severe phase decomposition at higher Mg contents; the LTP was completely decomposed at $x = 5$. The increased $(BH)_{max}$ for $Mn_{56}Bi_{44-x}Mg_x$ ($0 \leq x \leq 5$) is attributed to the enhanced squareness. However, the squareness monotonically decreased with increasing Mg content for $Mn_{56}Bi_{43.5-x}Sb_{0.5}Mg_x$ ($0 \leq x \leq 5$), resulting in decreased $(BH)_{max}$. The decreasing magnetization and increasing H_c for $x \geq 3$ are attributed to the existence of nonmagnetic secondary phases, which act as pinning centers for the domain walls.
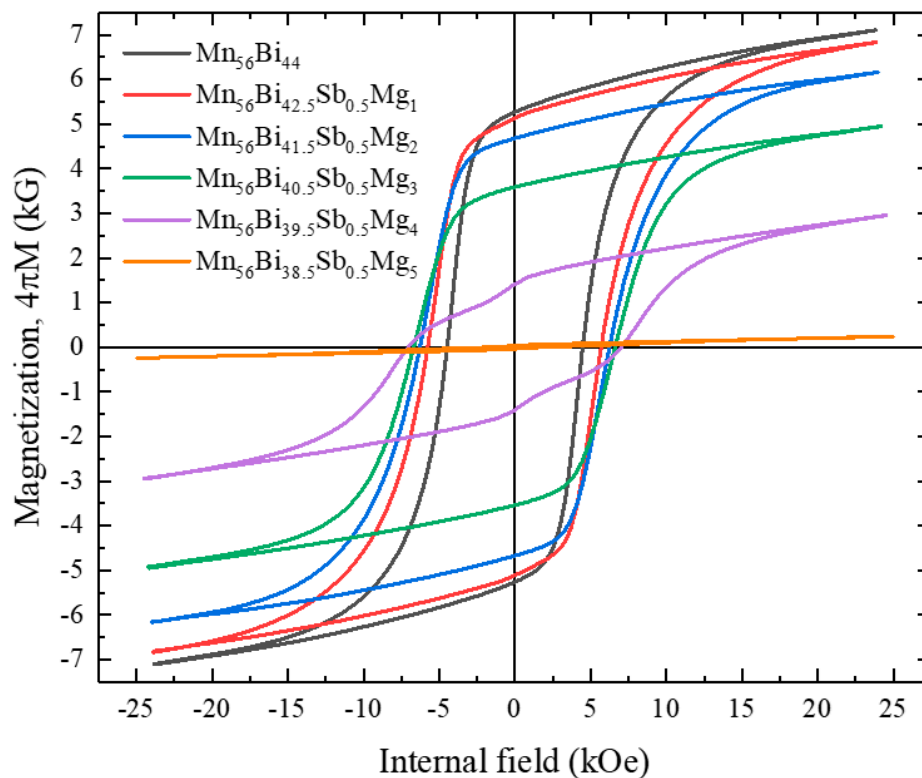

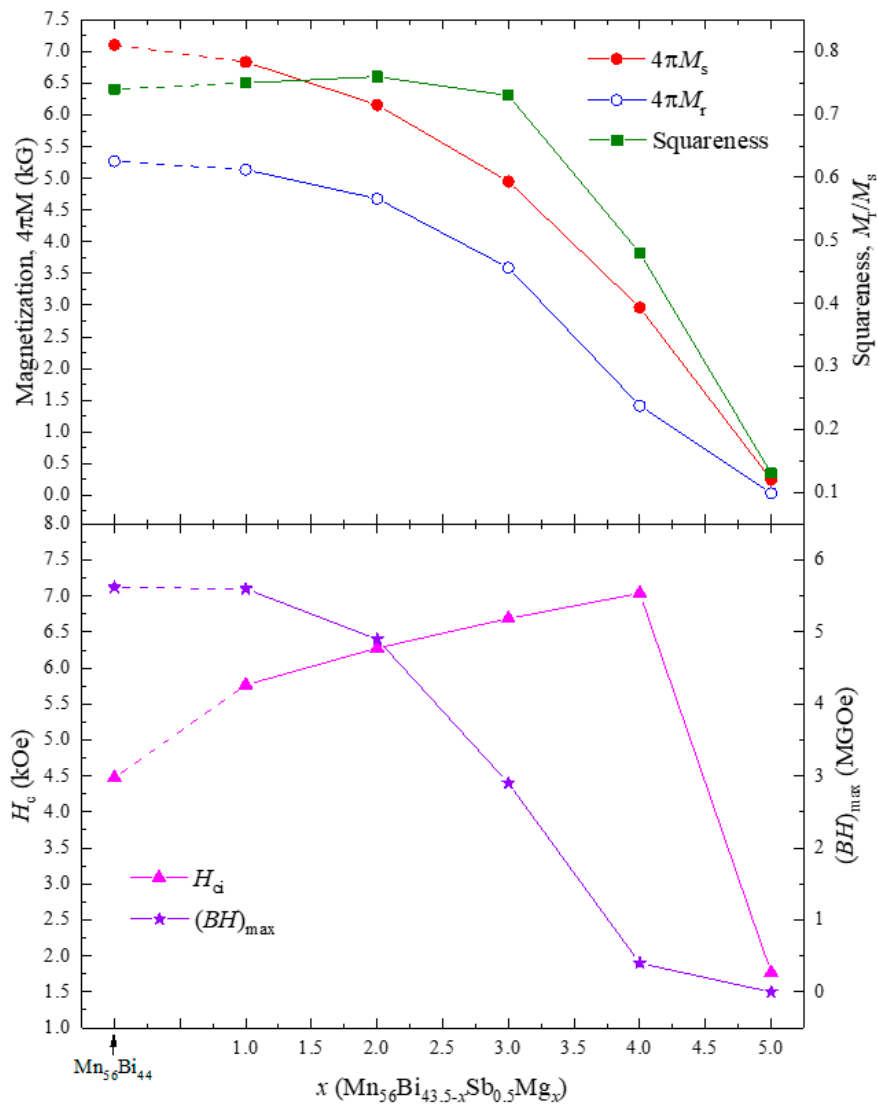**Figure 7.** Magnetic hysteresis loops of $Mn_{56}Bi_{43.5-x}Sb_{0.5}Mg_x$ ($0 \leq x \leq 5$) bulk samples.

Figure 8. Composition dependence of magnetization, squareness, H_c, and $(BH)_{max}$ for $Mn_{56}Bi_{43.5-x}Sb_{0.5}Mg_x$ ($0 \leq x \leq 5$) bulk samples.

The substitution effects of Mg and Sb on the magnetic properties of MnBi were also investigated using first-principles calculations. Mg and Sb are presumed to substitute in the Bi site in the unit cell of MnBi (Figure 1). The crystal structures of $Mn_{16}Bi_{15}Mg$ (or Sb) and $Mn_{16}Bi_{14}SbMg$ for the calculations are shown in Figure 9. Figure 10 shows the DOSs of LTP MnBi, $Mn_{16}Bi_{15}Mg$, $Mn_{16}Bi_{15}Sb$, and $Mn_{16}Bi_{14}SbMg$, which were calculated based on spin-polarized and spin-orbit coupling. The *s* bands of Bi, Mg, and Sb mainly contributed to the low-energy region below the Fermi energy (E_F), whereas the *d* band of Mn mainly contributed to the high-energy region above E_F, as seen in Figure 10. The DOS is a highly degenerate energy state that is slightly below and above E_F in the majority and minority spin states, respectively. These highly degenerate energy states near the E_F are the origin of the magnetic moment of LTP MnBi-based magnetic materials because they contribute to the difference between the number of electrons in the majority and minority spin states below the E_F. In contrast to the highly degenerate DOSs below (above) the E_F for the majority (minority) spin states of LTP MnBi, $Mn_{16}Bi_{15}Mg$, $Mn_{16}Bi_{15}Sb$, and $Mn_{16}Bi_{14}SbMg$ (see Figure 10), the E_F lies at the low DOS between the highly degenerated spin states for the majority and minority spin states. This E_F position is the origin of the phase stability of the above-mentioned LTP MnBi-based magnetic materials.
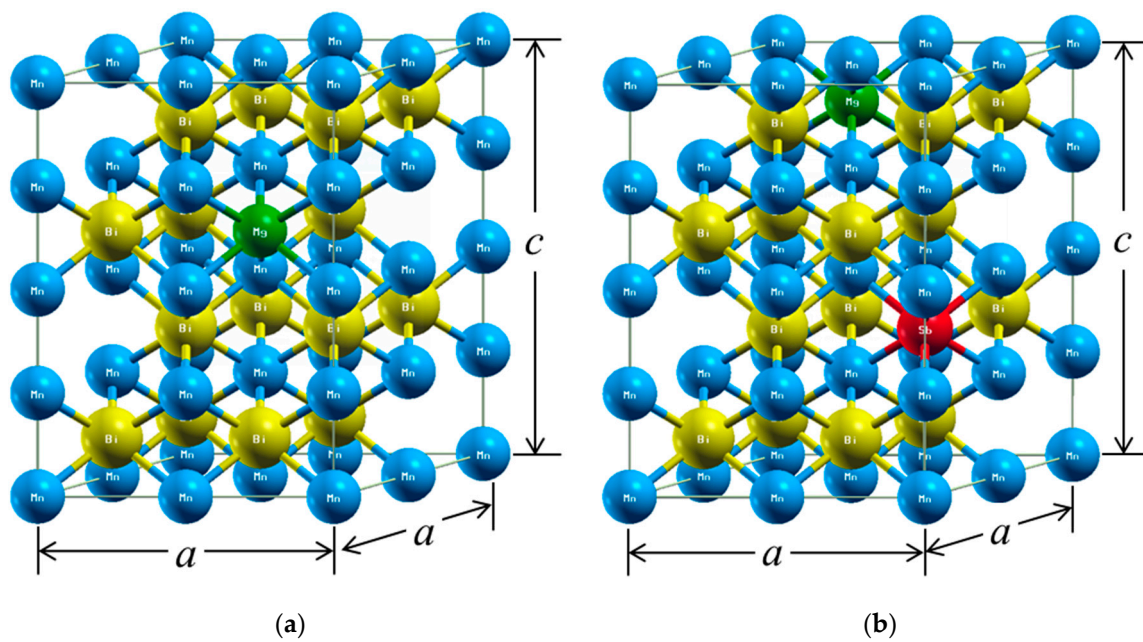
(**a**)　　　　　　　　　　　　　　(**b**)

Figure 9. Crystal structures of (**a**) $Mn_{16}Bi_{15}Mg$ (or Sb) and (**b**) $Mn_{16}Bi_{14}SbMg$ used for the first-principles calculations. The Mn, Bi, Mg, and Sb atoms are in blue, yellow, green, and red, respectively.
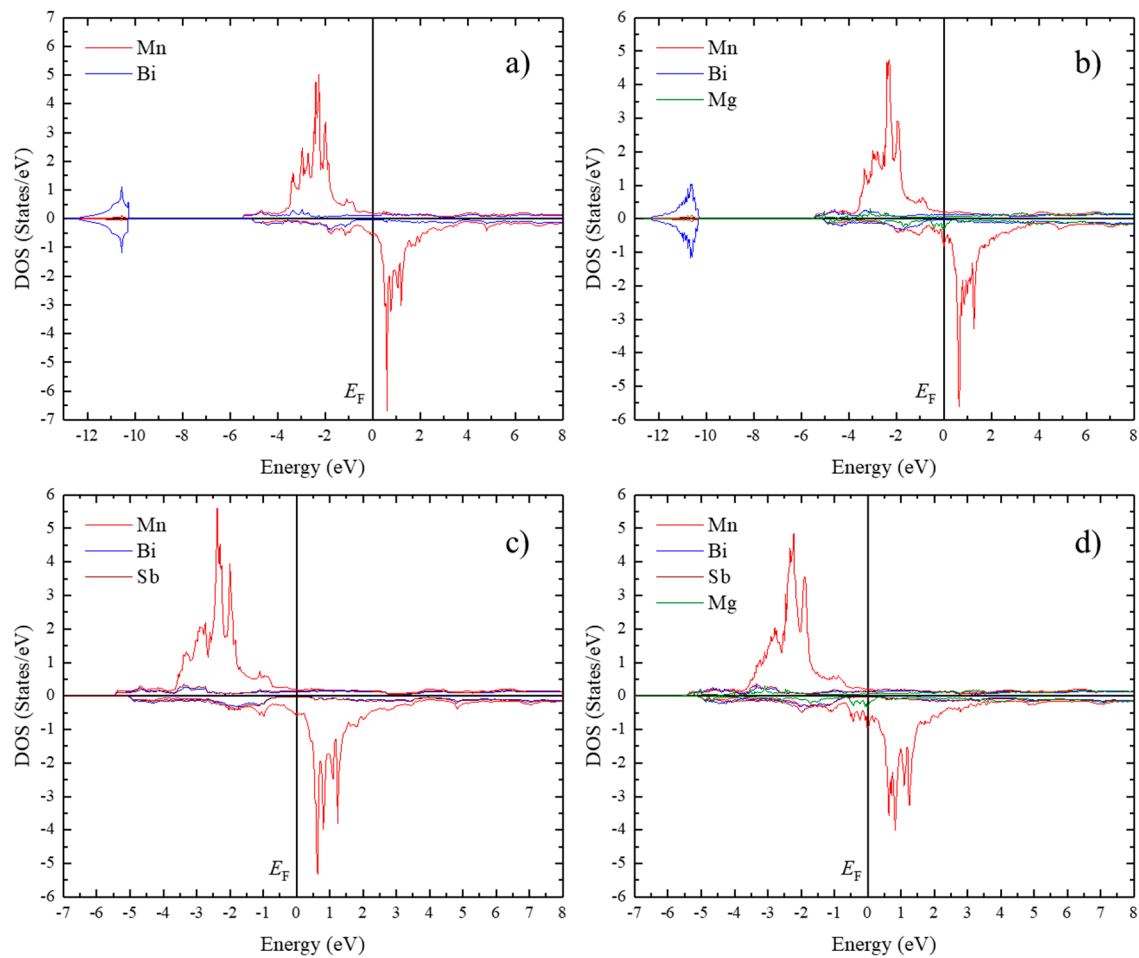

Figure 10. Density of states (DOS) for (**a**) MnBi, (**b**) $Mn_{16}Bi_{15}Mg$, (**c**) $Mn_{16}Bi_{15}Sb$, and (**d**) $Mn_{16}Bi_{14}SbMg$.

The spin magnetic moments for Mn, Bi, Mg, and Sb and the anisotropy constants (K) for MnBi, MnMg, $Mn_{16}Bi_{15}Mg$, $Mn_{16}Bi_{15}Sb$, and $Mn_{16}Bi_{14}SbMg$ are given in Table 1. The spins of the Mn atoms in MnMg were antiparallel to each other, resulting in a small total magnetic moment. The magnetic moment of Mn was approximately 3.57 μ_B, whereas those of Bi, Mg, and Sb were approximately −0.1 μ_B for all ferromagnetic MnBi-based materials, as shown in Table 1. Therefore, the magnetic properties of MnBi-based magnetic materials are mostly dependent on the Mn atoms. The total magnetic moments of a Mg or Sb element or a Mg/Sb pair-substituted MnBi were not degraded; the total magnetic moments of $Mn_{16}Bi_{15}Mg$, $Mn_{16}Bi_{15}Sb$, and $Mn_{16}Bi_{14}SbMg$ were similar to that of MnBi (56.352 μ_B = 7.044 μ_B × 8 unit cells).

Table 1. Calculated Mn, Bi, Mg, Sb, interstitial, and total magnetic moments and anisotropy constants.

Materials	Mn	Bi	Mg	Sb	Interstitial, Int.	Total Magnetic Moments, μ_B	Anisotropy Constant, K ($\times 10^6$ J/m^3)
MnBi	3.571	−0.103	-	-	0.104	7.044	−0.850
MnMg	2.331	-	0.002	-	0.006	0.067	19.690
$Mn_{16}Bi_{15}Mg$	3.577	−0.108	−0.071	-	0.790	56.371	−0.898
$Mn_{16}Bi_{15}Sb$	3.573	−0.121	-	−0.124	0.741	56.210	6.042
$Mn_{16}Bi_{14}SbMg$	3.579	−0.134	−0.071	−0.131	0.784	56.368	−0.441

The K value of MnBi was calculated to be $−0.850 \times 10^6$ J/m^3, which corresponds to an in-plane spin direction. The spins of MnBi at 0 K lie in the basal plane but rotate to the c-axis at approximately 90 K [9]. The K of Mg-substituted MnBi, i.e., $Mn_{16}Bi_{15}Mg$, was almost identical to that of pure MnBi, whereas that of Sb-substituted MnBi, i.e., $Mn_{16}Bi_{15}Sb$, was much larger than $Mn_{16}Bi_{15}Mg$ in the c-axis, as shown in Table 1. Therefore, one Mg element substitution into $Mn_{16}Bi_{16}$ resulted in no K change, whereas one Sb element substitution resulted in an out-of-plane spin direction; this property is necessary for the development of permanent magnets. Moreover, the K of 6.042×10^6 J/m^3 for $Mn_{16}Bi_{15}Sb$ is comparable to that of commercial rare-earth permanent magnets, such as 4.9×10^6 J/m^3 for $Nd_2Fe_{14}B$ and 4.2×10^6 J/m^3 for Sm_2Co_{17} [32]. In addition, the K of the Sb/Mg pair-substituted MnBi, i.e., $Mn_{16}Bi_{14}SbMg$, was larger than that of $Mn_{16}Bi_{15}Mg$ due to the substitution effect of Sb.

4. Conclusions

We optimized the initial Mn-Bi composition and annealing temperature for high-purity LTP using melt-spinning and annealing processes. The optimized annealing conditions were applied to fabricate Mg and Mg- and Sb-substituted Mn-Bi using magnetic annealing. The magnetic field annealing of $Mn_{56}Bi_{44}$ resulted in an enhanced squareness of 0.74, which was further increased to 0.8 upon Mg substitution. The highest coercivity and maximum energy product of Mg-substituted Mn-Bi were 9659 Oe (for $Mn_{56}Bi_{40}Mg_4$) and 5.64 MGOe (for $Mn_{56}Bi_{42}Mg_2$), respectively. First-principles calculations indicated that the total magnetic moments of $Mn_{16}Bi_{15}Mg$ and $Mn_{16}Bi_{15}Sb$ were similar to the total magnetic moment of pure $Mn_{16}Bi_{16}$. In contrast, the anisotropy constant K changed from −0.85 to 6.042 MJ/m^3 when Sb was substituted, indicating that the spin direction in the basal plane changed to the c-axis.

Author Contributions: Conceptualization, J.T.L.; Formal analysis, J.-W.K.; Investigation, H.-D.Q. and Y.Y.; Supervision, C.-J.C.; Writing—original draft, J.P.; Writing—review & editing, J.P. All authors have read and agreed to the published version of the manuscript.

Conflicts of Interest: The authors declare no conflict of interest. The sponsors had no involvement in the study design; in the collection, analysis, or interpretation of data; in the writing of the report; or in the decision to submit the article for publication.

References

1. Vagati, A. The Synchronous Reluctance Solution: A New Alternative in AC drives. In Proceedings of the IECON'94–20th Annual Conference of IEEE Industrial Electronics, Bologna, Italy, 5–9 September 1994; Volume 1, pp. 1–13.

2. Lipo, T.A. Synchronous reluctance machines-a viable alternative for AC drives? *Electr. Mach. Power Syst.* **1991**, *19*, 659–671. [CrossRef]

3. Rama Rao, N.V.; Gabay, A.M.; Hadjipanayis, G.C. Anisotropic fully dense MnBi permanent magnet with high energy product and high coercivity at elevated temperatures. *J. Phys. D Appl. Phys.* **2013**, *46*, 062001. [CrossRef]

4. Cao, J.; Huang, Y.L.; Hou, Y.H.; Shi, Z.Q.; Yan, X.T.; Zhong, Z.C.; Wang, G.P. Microstructure and magnetic properties of MnBi alloys with high coercivity and significant anisotropy prepared by surfactant assisted ball milling. *J. Magn. Magn. Mater.* **2019**, *473*, 505–510. [CrossRef]

5. Chinnasamy, C.; Jasinski, M.M.; Ulmer, A.; Li, W.; Hadjipanayis, G.; Liu, J. Mn-Bi magnetic powders with high coercivity and magnetization at room temperature. *IEEE Trans. Magn.* **2012**, *48*, 3641–3643. [CrossRef]

6. Yang, Y.; Park, J.; Lim, J.T.; Kim, J.-W.; Li, O.L.; Choi, C.-J. Effect of phase purity on enhancing the magnetic properties of Mn-Bi alloy. *J. Magn. Magn. Mater.* **2021**, *517*, 167344. [CrossRef]

7. Cui, J.; Choi, J.P.; Li, G.; Polikarpov, E.; Darsell, J.; Overman, N.; Olszta, M.; Schreiber, D.; Bowden, M.; Droubay, T.; et al. Thermal stability of MnBi magnetic materials. *J. Phys. Condens. Matter* **2014**, *26*, 064212. [CrossRef]

8. Kim, S.; Moon, H.; Jung, H.; Kim, S.-M.; Lee, H.-S.; Choi-Yim, H.; Lee, W. Magnetic properties of large-scaled MnBi bulk magnets. *J. Alloys Compd.* **2017**, *708*, 1245–1249. [CrossRef]

9. Yang, J.B.; Yelon, W.B.; James, W.J.; Cai, Q.; Kornecki, M.; Roy, S.; Ali, N.; L'Heritier, P. Crystal structure, magnetic properties and electronic structure of the MnBi intermetallic compound. *J. Phys. Condens. Matter* **2002**, *14*, 6509–6519. [CrossRef]

10. Poudyal, N.; Liu, X.; Wang, W.; Nguyen, V.V.; Ma, Y.; Gandha, K.; Elkins, K.; Liu, J.P.; Sun, K.; Kramer, M.J.; et al. Processing of MnBi bulk magnets with enhanced energy product. *AIP Adv.* **2016**, *6*, 056004. [CrossRef]

11. Park, J.; Hong, Y.-K.; Lee, J.; Lee, W.; Kim, S.-G.; Choi, C.-J. Electronic structure and maximum energy product of MnBi. *Metals* **2014**, *4*, 455–464. [CrossRef]

12. Yang, Y.; Kim, J.-W.; Si, P.-Z.; Qian, H.-D.; Shin, Y.; Wang, X.; Park, J.; Li, O.L.; Wu, Q.; Ge, H.; et al. Effects of Ga-doping on the microstructure and magnetic properties of MnBi alloys. *J. Alloys Compd.* **2018**, *769*, 813–816. [CrossRef]

13. Sakuma, A.; Manabe, Y.; Kota, Y. First principles calculation of magnetocrystalline anisotropy energy of MnBi and MnBi$_{1-x}$Sn$_x$. *J. Phys. Soc. Jpn.* **2013**, *82*, 073704. [CrossRef]

14. Qian, H.-D.; Park, J.; Lim, J.T.; Yang, Y.; Si, P.-Z.; Kim, J.W.; Choi, C.-J.; Cho, K.M. Magnetic properties of MnBi bulk magnets with NaCl and C addition. *AIP Adv.* **2019**, *9*, 115213. [CrossRef]

15. Wang, X.; Qian, H.; Si, P.-Z.; Yang, Y.; Choi, C.-J.; Park, J.; Wang, X.; Ge, H.; Shinde, K.P.; Chung, K. Structure and magnetic properties of MnBi nanoparticles prepared by laser ablation and arc-discharge method. *IEEE Trans. Magn.* **2018**, *54*, 2301005. [CrossRef]

16. Yasuda, H.; Ohnaka, I.; Yamamoto, Y.; Tokieda, K.; Kishio, K. Formation of crystallographically aligned BiMn grains by semi-solid processing of rapidly solidified Bi-Mn alloys under a magnetic field. *Mater. Trans.* **2003**, *44*, 2207–2212. [CrossRef]

17. Ren, Z.-M.; Li, X.; Deng, K.; Wang, H.; Zhuang, Y. Solidification structures of Bi-Mn alloys under a high magnetic field. *J. Shanghai Univ.* **2006**, *10*, 74–77. [CrossRef]

18. Kobayashi, R.; Mitsui, Y.; Takahashi, K.; Uda, S.; Koyama, K. In-field annealing and quenching for ferromagnetic MnBi under 19 T. *IEEE Trans. Magn.* **2019**, *55*, 1000204. [CrossRef]

19. Mitsui, Y.; Abematsu, K.; Umetsu, R.Y.; Takahashi, K.; Koyama, K. Magnetic field effects on liquid-phase reactive sintering of MnBi. *J. Magn. Magn. Mater.* **2016**, *400*, 304–306. [CrossRef]

20. Zhang, W.Y.; Kharel, P.; George, T.; Li, X.Z.; Mukherjee, P.; Valloppilly, S.; Sellmyer, D.J. Grain alignment due to magnetic-field annealing in MnBi:Bi nanocomposites. *J. Phys. D Appl. Phys.* **2016**, *49*, 455002. [CrossRef]

21. Si, P.Z.; Yang, Y.; Yao, L.L.; Qian, H.D.; Ge, H.L.; Park, J.; Chung, K.C.; Choi, C.J. Magnetic-field-enhanced reactive synthesis of MnBi from Mn nanoparticles. *J. Magn. Magn. Mater.* **2019**, *476*, 243–247. [CrossRef]

22. Mishima, T. Magnet Steel Containing Nickel and Aluminium. U.S. Patent 2,027,994, 14 January 1936.

23. Zhang, W.; Balasubramanian, B.; Kharel, P.; Pahari, R.; Valloppilly, S.R.; Li, X.; Yue, L.; Skomski, R.; Sellmyer, D.J. High energy product of MnBi by field annealing and Sn alloying. *APL Mater.* **2019**, *7*, 121111. [CrossRef]

24. Gabay, A.M.; Hadjipanayis, G.C.; Cui, J. Effect of Sb substitution on crystal structure, texture and hard magnetic properties of melt-spun MnBi alloys. *J. Alloys Compd.* **2019**, *792*, 77–86. [CrossRef]

25. Gabay, A.M.; Hadjipanayis, G.C.; Cui, J. New anisotropic MnBi permanent magnets by field-annealing of compacted melt-spun alloys modified with Mg and Sb. *J. Magn. Magn. Mater.* **2020**, *495*, 165860. [CrossRef]

26. Gabay, A.M.; Hadjipanayis, G.C. Effect of Mg content in melt-spun Mn–Bi–Mg–Sb–In alloys on the structure and properties of field-annealed magnets. *IEEE Magn. Lett.* **2020**, *11*, 7503304. [CrossRef]

27. Gabay, A.M.; Hadjipanayis, G.C.; Cui, J. Development of rare-earth-free bulk magnets with energy product up to 12 MGOe in field annealed Mn–Bi–Mg–In–Sb alloys. *J. Alloys Compd.* **2020**, *822*, 153663. [CrossRef]

28. Blaha, P.; Schwarz, K.; Madsen, G.; Kvasnicka, D.; Luitz, J. *WIEN2k: An Augmented Plane Wave Plus Local Orbitals Program for Calculating Crystal Properties*; Vienna University of Technology: Vienna, Austria, 2001.

29. Roberts, B.W. Neutron diffraction study of the structures and magnetic properties of manganese bismuthide. *Phys. Rev.* **1956**, *104*, 607–616. [CrossRef]

30. Chen, T. Contribution to the equilibrium phase diagram of the Mn-Bi system near MnBi. *J. Appl. Phys.* **1974**, *45*, 2358–2360. [CrossRef]

31. Christopher, N.R.; Singh, N.; Singh, S.K.; Gahtori, B.; Mishra, S.K.; Dhar, A.; Awana, V.P.S. Appreciable magnetic moment and energy density in single-step normal route synthesized MnBi. *J. Supercond. Novel Magn.* **2013**, *26*, 3161–3165. [CrossRef]

32. Coey, J.M.D. *Magnetism and Magnetic Materials*, 1st ed.; Cambridge University Press: Cambridge, UK, 2009; pp. 401–404.